



JGR Solid Earth



RESEARCH ARTICLE

10.1029/2022JB024814

Locally Resolved Stress-State in Samples During Experimental Deformation: Insights Into the Effect of Stress on Mineral Reactions

S. Cionoiu¹ , E. Moulas², H. Stünitz^{3,4} , and L. Tajčmanová¹

¹Institute of Earth Sciences, Heidelberg University, Heidelberg, Germany, ²Institute of Geosciences, Johannes Gutenberg University Mainz, Mainz, Germany, ³Department of Geosciences, Arctic University of Norway, Tromsø, Norway, ⁴Institute of Earth Sciences, University of Orléans, Orléans, France

Key Points:

- Heterogeneous stress distribution in deformation experiments is investigated by numerical models, locally resolving mechanical variables
- Resolving the mechanical variables in experiments suggests a link between local pressure (mean stress) variations and phase transition
- Thermodynamic interpretations of deformed samples require a detailed understanding of local mechanical parameters

Supporting Information:

Supporting Information may be found in the online version of this article.

Correspondence to:

S. Cionoiu,
sebastian.cionoiu@geow.uni-heidelberg.de

Citation:

Cionoiu, S., Moulas, E., Stünitz, H., & Tajčmanová, L. (2022). Locally resolved stress-state in samples during experimental deformation: Insights into the effect of stress on mineral reactions. *Journal of Geophysical Research: Solid Earth*, 127, e2022JB024814. <https://doi.org/10.1029/2022JB024814>

Received 19 MAY 2022

Accepted 12 AUG 2022

Author Contributions:

Conceptualization: S. Cionoiu, L. Tajčmanová
Funding acquisition: L. Tajčmanová
Investigation: S. Cionoiu
Methodology: S. Cionoiu, E. Moulas, L. Tajčmanová
Supervision: E. Moulas, H. Stünitz, L. Tajčmanová
Validation: E. Moulas, H. Stünitz
Visualization: S. Cionoiu
Writing – original draft: S. Cionoiu
Writing – review & editing: S. Cionoiu, E. Moulas, H. Stünitz, L. Tajčmanová

Abstract Understanding conditions in the Earth's interior requires data derived from laboratory experiments. Such experiments provide important insights into the conditions under which mineral reactions take place as well as processes that control the localization of deformation in the deep Earth. We performed Griggs-type general shear experiments in combination with numerical models, based on continuum mechanics, to quantify the effect of evolving sample geometry of the experimental assembly. The investigated system is constituted by CaCO₃ and the experimental conditions are near the calcite-aragonite phase transition. All experimental samples show a heterogeneous distribution of the two CaCO₃ polymorphs after deformation. This distribution is interpreted to result from local stress variations. These variations are in agreement with the observed phase-transition patterns and grain-size gradients across the experimental sample. The comparison of the mechanical models with the sample provides insights into the distribution of local mechanical parameters during deformation. Our results show that, despite the use of homogeneous sample material (here calcite), stress variations develop due to the experimental geometry. The comparison of experiments and numerical models indicates that aragonite formation is primarily controlled by the spatial distribution of mechanical parameters. Furthermore, we monitor the maximum pressure and σ_1 that is experienced in every part of our model domain for a given amount of time. We document that local pressure (mean stress) values are responsible for the transformation. Therefore, if the role of stress as a thermodynamic potential is investigated in similar experiments, an accurate description of the state of stress is required.

Plain Language Summary To understand processes in the Earth's interior, we can simulate the extreme conditions via laboratory experiments by compressing and heating millimeter-sized samples. Such experiments provide important insights into mineral reactions and processes that control deformation in the Earth. We performed rock deformation experiments close to calcite-aragonite phase (CaCO₃) transition. Deforming the sample leads to stress variations due to the experimental geometry. These variations are documented by locally occurring phase transition and variation in the grain-size. We performed computer simulations of the deforming sample to quantify, for the first time, the effect of sample geometry on the distribution of mechanical variables, such as stress, pressure, or deformation, inside the sample. The new findings document that any mechanical variable cannot be treated as homogeneous within the sample because the variations can be significant. Deforming the sample leads to stress concentrations. By comparing the experimental observations and simulation results, we show that locally high pressure triggers the phase transition to aragonite, the high-pressure polymorph. This has important consequences for further thermodynamic interpretations of systems under stress, where the role of deformation, pressure, or maximum principal stress on mineral reactions is investigated.

1. Introduction

Understanding how geological materials respond to deformation helps us to reconstruct and predict geodynamic processes as well as natural hazards. Deformation experiments are required to simulate the pressure (P), temperature (T), and mechanical conditions that occur below the Earth's surface. The flow of rocks and the corresponding deformation rates are primarily dependent on stress, temperature, and confining pressure (e.g., Karato, 2008; Paterson & Wong, 2005). In fact, high temperatures favor viscous deformation, where the stress that is experienced by the rock is proportional to the strain rate. Experiments performed at high pressure and temperature

© 2022. The Authors.

This is an open access article under the terms of the [Creative Commons Attribution License](https://creativecommons.org/licenses/by/4.0/), which permits use, distribution and reproduction in any medium, provided the original work is properly cited.

conditions (HP-HT) provide not only mechanical data (e.g., stress and strain rate) but also influence the rock microstructure (i.e., changes in grain-size; e.g., Griggs, 1940; Schmid et al., 1980; Poirier, 1985; Paterson & Wong, 2005). The experimentally produced microstructures can be studied to gain insights into deformation mechanisms and be compared with naturally deformed samples to ensure the applicability of the laboratory results to nature. For example, the relation between stress and grain-size has been used as paleo-piezometer to infer stress conditions in natural microstructures (e.g., Rutter, 1995; Schmid et al., 1980).

A common assumption in coaxial shortening and general shear deformation experiments is that the state of stress can be treated as homogeneous within the sample, thus leading to spatially homogeneous strain rates. However, several studies have documented the heterogeneous distribution of high-pressure polymorphs (e.g., quartz/coesite) in deforming samples that experienced phase transitions (Green, 1972; Hirth & Tullis, 1994; Hobbs, 1968; Richter et al., 2016; Zhou et al., 2005). Interestingly, all these studies demonstrated that the crystallization of the high-pressure polymorph is not a simple function of the confining pressure but it rather occurs in non-hydrostatically stressed samples. In particular, the maximum principal stress (σ_1) in the deformed samples reached a value equal to or greater than the phase transition pressure (P_{trans}). On the one hand, this observation has led to interpretations, where the experimentally determined σ_1 has a major impact on mineral reactions and phase transitions (e.g., Paterson, 1973; Wheeler, 2014). On the other hand, theoretical studies suggest that the heterogeneous nucleation of high-pressure polymorphs is related to the spatially heterogeneous strain or pressure (Ji & Wang, 2011; Moulas et al., 2013). Recently, the combination of deformation experiments together with numerical modeling of rock deformation confirmed the presence of stress and pressure variations during coaxial shortening of heterogeneous samples (Cionoiu et al., 2019). This work qualitatively related these variations to locally occurring phase transitions. Based on these new findings, it is essential to be able to quantify the heterogeneity of mechanical parameters in order to quantify the stress/pressure distribution. Complex thermodynamic interpretations must be based on mechanically valid observations/sample models.

In this contribution, we build on the recent findings of Cionoiu et al. (2019) and present combined numerical models and deformation experiments to quantify the effect of evolving sample geometry on the heterogeneous distribution of mechanical parameters such as differential stress and mean stress. We use a simple CaCO_3 system in general shear experiments and analyze the spatially inhomogeneous crystallization of aragonite at conditions where the confining pressure favors calcite formation. Furthermore, we relate the observed heterogeneous grain-size distribution in the experimental samples to the modeled (heterogeneously distributed) differential stress. Our combined results suggest that the evolving sample geometry is responsible for significant variations in all mechanical parameters that need to be considered in deformation experiments. Moreover, the evolution of the locally resolved pressure in time explains the spatial distribution of the two polymorphs within the sample. Therefore, any thermodynamic interpretation of a stressed system must take into account the locally resolved state of stress during sample deformation.

2. Methods

2.1. Deformation Experiments and Sample Preparation

General shear deformation experiments were carried out in Griggs-type deformation apparatuses installed at the ETH Zurich and University Tromsø (UiT) using a solid salt sample assembly (Tullis & Tullis, 1986). The detailed experiment conditions are shown in Table S1 in Supporting Information S1. We followed the preparation, experimental, and correction procedure after Richter et al. (2016), and the adapted techniques are listed below. The sample material was either Carrara Marble (samples 022SC–026SC) or natural calcite-powder (524SC–530SC and 001–008SC), which was sieved to 63–125 μm and not washed. The natural powder was obtained from crushing a high purity Iceland spar single crystal (from Helgustadir, Iceland). Both sample materials were dried at 110°C. In addition, the material for 511SC was a clear calcite crystal that was crushed to <0.5 mm, neither sieved nor dried. 0.1 μl of H_2O was added to all samples with a calcite mass of 98–103 mg (i.e., ~0.1 wt%). The sample material was placed between two alumina (Al_2O_3) forcing blocks that were pre-cut at 45° relative to the vertical displacement direction, within a 0.15 mm thick welded Pt-capsule (Figure 1a). To obtain this configuration, the lower forcing block was introduced into the jacket, then the powder was added and pre-compressed at a 45° angle. After adding water, the second forcing block was placed on top and the capsule was welded. The expected shear direction was marked on the jacket and the thermocouple was placed at the side of the shear zone in a central position. Each assembly was hot-pressed for 13–15 hr at 600°C and experimental confining pressure before

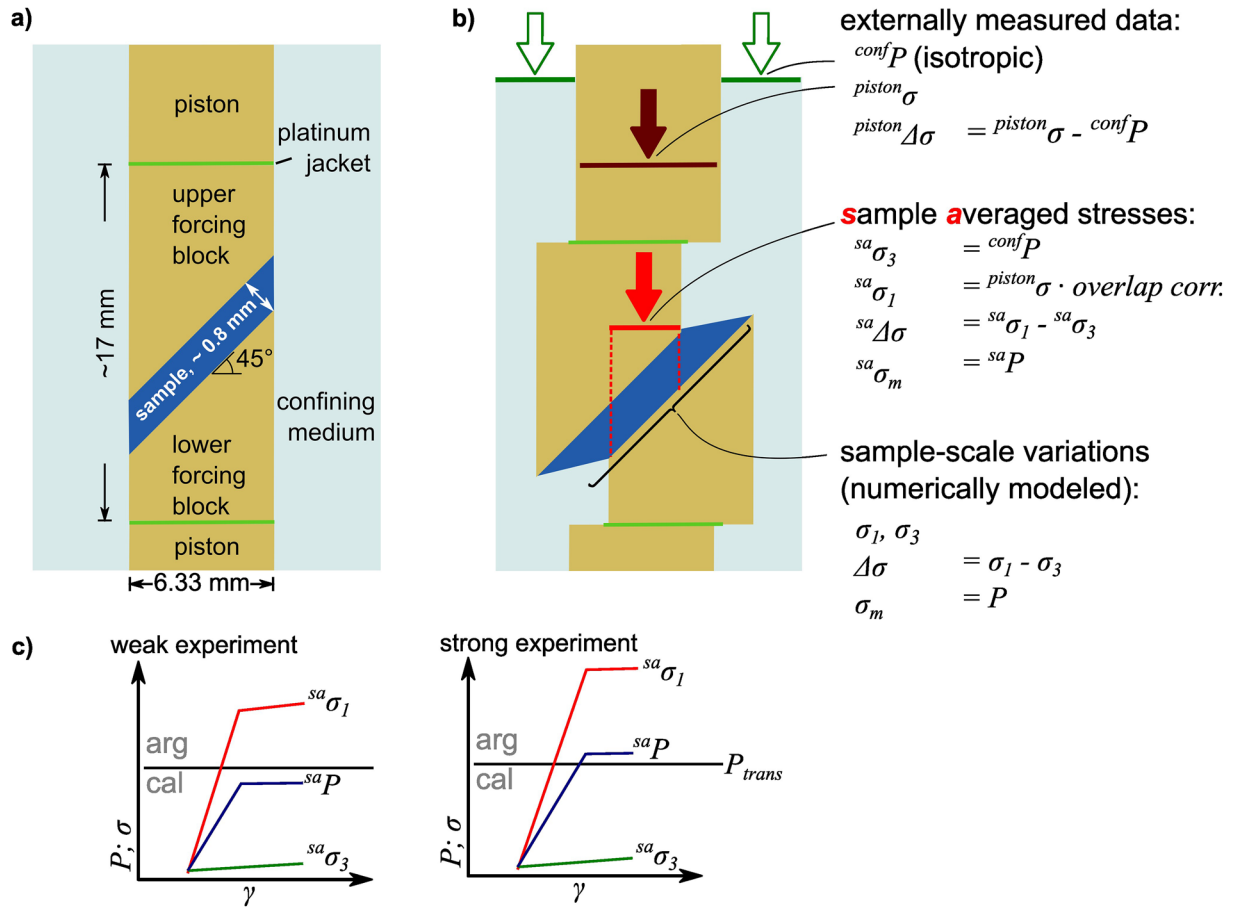


Figure 1. Sketch of the experimental configuration and terminology followed in this study. (a) Initial sample configuration (undeformed). The starting sample material is calcite, pistons, and forcing-blocks are made from alumina (Al_2O_3), and the confining medium is potassium iodide (KI). The platinum jacket covers the whole sample. For clarity, only the sliding part is shown, because this strongly influences the sample deformation. (b) Sample configuration at the end of an experiment with a description of the (scale-dependent) terminology for stresses used in this paper. We use left-side superscripts to indicate the location to which mechanical variables refer (confining medium, piston, sample-average). The sample averaged values are those commonly published in the experimental literature and represent the stress state of a homogeneously stressed and deforming material confined between the decreasing overlap area of the forcing blocks. σ_m denotes the mean stress equal to P . The actual stress data of the sample are indicated without superscript. All compressive stresses are positive by definition. (c) Expected stress-strain evolution during an experiment that is set up at confining pressure closely below the phase transition. Weak experiments (low ${}^{sa}\Delta\sigma$) reach ${}^{sa}P$ below P_{trans} . Strong experiments (high ${}^{sa}\Delta\sigma$), the ${}^{sa}P$ is overstepping P_{trans} . P_{trans} is phase transition pressure at given temperature.

deformation. After the deformation experiment, the sample was quenched from 600°C to 200°C at a rate of 25°C/s to prevent back-reactions and preserve any transformed phases.

In this work, the sample-average mechanical variables (classically reported in experimental rock-deformation literature) are indicated by “sa” superscripts (Figure 1b). The measurements of the confining pressure in both machines were corrected as shown in Text S2 in Supporting Information S1. The mechanical experimental data (stress and displacement) were corrected using the RIG AB program (Heilbronner et al., 2020; Richter et al., 2016). This includes corrections for: decreasing piston-overlap area, friction during lead run-in, and deformation and machine compliance. Furthermore, the “classical” hit point was used (see Figure 3 in Richter et al., 2016), and ${}^{sa}\sigma_1$ was set equal to ${}^{sa}\sigma_3 (= {}^{conf}P)$ at this point. The variations of ${}^{sa}\sigma_3$ during deformation were evaluated beyond this point. In particular, the externally measured force (F) is recalculated to sample averaged stress (${}^{sa}\sigma_1 = F/A$) where A is decreasing over time, thus accounting for the decreasing forcing-block sample overlap. Following the convention in experimental literature, all stresses (including pressure) are taken as positive in compression.

The mechanical data (e.g., stress and strain rate) derived from Griggs-rig experiments represent the average state of an idealized, homogeneously stressed, and deforming shear zone. Simple geometrical corrections are

commonly applied to extract the sample-averaged stress and strain-rate values (Heilbronner et al., 2020; Richter et al., 2016). Thus, approximations for the pressure (i.e., mean stress) within the sample need to be made considering the particular aspects of the flow in general shear. The sample-average pressure (mean stress) is then given by (see Text S3 in Supporting Information S1 for details):

$${}^{sa}P = \frac{{}^{sa}\sigma_1 + {}^{sa}\sigma_3}{2} \quad (1)$$

This equation suggests that the pressure of the sample depends not only on the confining pressure ${}^{conf}P = {}^{sa}\sigma_3$ but also on the maximum principal stress ${}^{sa}\sigma_1$. The confining pressure during the experiments was preferentially chosen to be below the phase transition pressure (calcite-aragonite) (${}^{sa}\sigma_3$ in Figure 1c). Similarly, the sample-average differential stress is given by:

$${}^{sa}\Delta\sigma = {}^{sa}\sigma_1 - {}^{sa}\sigma_3 \quad (2)$$

Therefore, the sample-average pressure ${}^{sa}P$ may be above or below P_{trans} depending on ${}^{sa}\sigma_3$ and the ${}^{sa}\Delta\sigma$, which is reflecting the strength of the analyzed sample (Figure 1c).

After recovery from the assembly, the samples were cut in half, mounted in Acryl (Struers Specifast), and polished with diamond paste (down to 0.25 μm) for reflected light microscopy and Raman spectroscopic analysis. For Electron Backscatter Diffraction analysis (EBSD), an additional polishing step with colloidal silica (Struers OP-U non-dry) was performed.

2.2. Raman Spectroscopy

Raman spectroscopic mapping was used to locally resolve the distribution of calcite and aragonite after the experiment. Raman mapping was carried out using a WITec Alpha 300R microscope and UHTS 300 Spectrometer VIS-NIR at Heidelberg University. The x - y stage was operated at a step-size of 8 μm . A 50 \times objective and a grating of 1,200 grooves/mm were used. The excitation laser wavelength was 531.98 nm. The laser intensity at the sample was 50 mW, which allows distinguishing calcite and aragonite spectra with 0.33 s acquisition time. For the map interpretation at each pixel, the spectra were analyzed and assigned to calcite (peak at 283 and 713 cm^{-1} ; Biellmann & Gillet, 1992), aragonite (peak at 209 and 706 cm^{-1} , Biellmann & Gillet, 1992) or a mix. The intensity of the different aragonite and calcite peaks varies with crystal-orientation and thus allows an approximate assessment of crystal coherence and size.

2.3. Electron Backscatter Detection

A field emission gun scanning electron microscope (JEOL IT800) at the Heidelberg University, equipped with an Oxford Instruments Symmetry2 EBSD was used for the EBSD analysis. The machine was operated in high vacuum mode, with 18 kV acceleration voltage, ca. 50 nA beam current, an aperture of 30 μm and sample tilt of 70°. The patterns were binned to 156 \times 128 px and dynamic background correction was applied. The orientation data were pre-processed in Aztec crystal (auto-clean), by removing wild spikes and applying a Kuwahara filter and merging twinned grains (plane orientation). Grain-size (area-equivalent diameter) maps and distributions were calculated using the MTEX toolbox (Hielscher & Schaeben, 2008), with a grain-boundary angle of $>7^\circ$. For discrete values, we report the modal value of a Weibull fit to the grain-size distribution.

2.4. Numerical Modeling of Sample Deformation

The actual variations of mechanical variables within the sample cannot be resolved in a deformation apparatus and therefore, sample-average values are used. To compute these local variations in the sample throughout the experiment, a numerical model is performed.

We used a finite difference numerical model to calculate the local mechanical variables (e.g., stress and strain rate) within the experimental assembly (Cionoiu et al., 2022). The model has a numerical resolution of 551 \times 851 grid points. We solve Stokes' equations for slow, viscous, incompressible flow. The code uses the MATLAB® direct solver, employs a staggered grid for discretization and the marker in cell method for model advection (Gerya & Yuen, 2003). For characteristic timescales that are larger than the effective viscoelastic deformation

timescale, the incompressible approximation yields accurate stress/pressure values (fig. 5 in Moulas et al., 2019). For the conditions of interest, the characteristic timescale of a purely viscous but elastically compressible material is ~ 100 s, which is much smaller than the simulated time. The model represents a cross section through the experiment in the e_1 – e_3 plane and it resolves the stress distribution within the forcing blocks and sheared calcite. This also allows the investigation of the influence of the confining medium and jacket deformation between the pistons and forcing blocks (see numerical results). Our experimentally determined and previously modeled temperature gradients indicate a variation of ca. 5% over the vertical distance of the sample, which does not affect the distribution of phases in experiments under stress (Cionoiu et al., 2019). Therefore, temperature is assumed to be homogeneously distributed and constant during deformation.

The boundaries of the model domain are extended to include the forcing blocks, pistons, and the confining medium (salt). In this way, the sample is at the center of the model domain and no boundary conditions are imposed on the sample directly. This treatment allows the simulation of more realistic boundary conditions on the sample (e.g., shape changes due to friction). Boundary conditions were set to free slip at the sides and top of the extended model, while the bottom was set to no-slip. An internal zone of constant vertical and zero horizontal displacement rate was set in the upper alumina piston. To control the overall deformation rate of the sample region, a uniform displacement rate in vertical direction is defined for experiments that produced symmetric thinning. The asymmetric thinning is produced by superimposing a lateral change in vertical velocity across the top piston that ranges from 1 (left) to 1.12 (right) of the base deformation rate. Within 600 calculation steps, a bulk shear strain of $\gamma = 4.0$ was reached.

The rheology of the sample materials was modeled using a power-law viscosity recalculated to strain-rate dependent effective viscosity using the relationships between stress and strain invariants and experimentally derived values described in Gerya (2009). For rheologies derived from either coaxial or for simple shear experiments Equation 3 and Equation 4 are used, respectively.

$$\eta_{\text{eff}} = \frac{1}{2^{(n-1)/n} 3^{(n+1)/2n}} \times \frac{1}{A^{1/n} \dot{\epsilon}_{II}^{(n-1)/n}} \times \exp\left(\frac{Q}{nRT}\right) \quad (3)$$

$$\eta_{\text{eff}} = \frac{1}{2^{(2n-1)/n}} \times \frac{1}{A^{1/n} \dot{\epsilon}_{II}^{(n-1)/n}} \times \exp\left(\frac{Q}{nRT}\right) \quad (4)$$

where η_{eff} (Pa s) is the effective viscosity; $\dot{\epsilon}_{II}$ (s^{-1}) is the second strain rate invariant, R (kJ/(mol K)) is the universal gas constant, n is the stress exponent, T (K) is temperature, Q (kJ/mol) is the activation energy, and A ($\text{Pa}^{-n} \text{s}^{-1}$) is a material parameter. The parameters we used for the different materials are described below.

We focused on modeling the deformation experiments in the CaCO_3 system that were performed in this study. In addition, we used the same numerical approach to model the results published for the SiO_2 system (Richter et al., 2016, 2018) for comparison. The flow law of Schmid et al. (1980) for Carrara Marble is used for calcite (Regime 2; $n = 7.6$, $A = 3.16 \times 10^{-43}$, $Q = 418.4$ in Equation 3). For temperatures of 600°C and strain rates of ca. 10^{-6} s^{-1} , differential stress is approximately 100–300 MPa. Under these conditions, the strengths of aragonite and calcite marbles are comparable for similar grain-size (50–100 μm ; Rybacki et al., 2003). For the quartz samples, we use the stress exponent derived by Richter et al. (2018) for their experiments and merge the temperature sensitivity together with the pre-exponential factor as only one temperature is analyzed. The effective pre-exponential factor A was calculated to fit the experimentally determined stress-strain relation ($n = 1.9$, $A = 9.46 \times 10^{-22}$; $Q = 0$ in Equation 4).

For the salt that is used as confining medium and the platinum jacket surrounding the sample, we employ temperature-dependent power-law. The flow law parameters for salt and platinum are based on Frost and Ashby (1982). The pre-exponential factor was adjusted to fit their deformation maps in the region of interest ($\dot{\gamma}$: 10^{-3} – 10^{-6} and T : 500 – 800°C). For platinum, the parameters of silver are used (both face-centered cubic metals) which approximate its behavior best, based on experimental observations ($n = 4.3$, $A = 8.77 \times 10^{-30}$, $Q = 100$ in Equation 3). For KI-salt, the material strength was reduced to 30% of NaCl-salt strength (Inoue, 1957; Pec et al., 2012) by modifying A ($n = 3.6$, $Q = 205$; for NaCl: $A = 4.64 \times 10^{-15}$; for KI: $A = 3.60 \times 10^{-13}$ in Equation 3). The viscosity of the non-deforming alumina parts (pistons and forcing blocks) was assumed to be constant with 10^{16} Pa s, that is, at least two orders of magnitude higher than the surrounding materials.

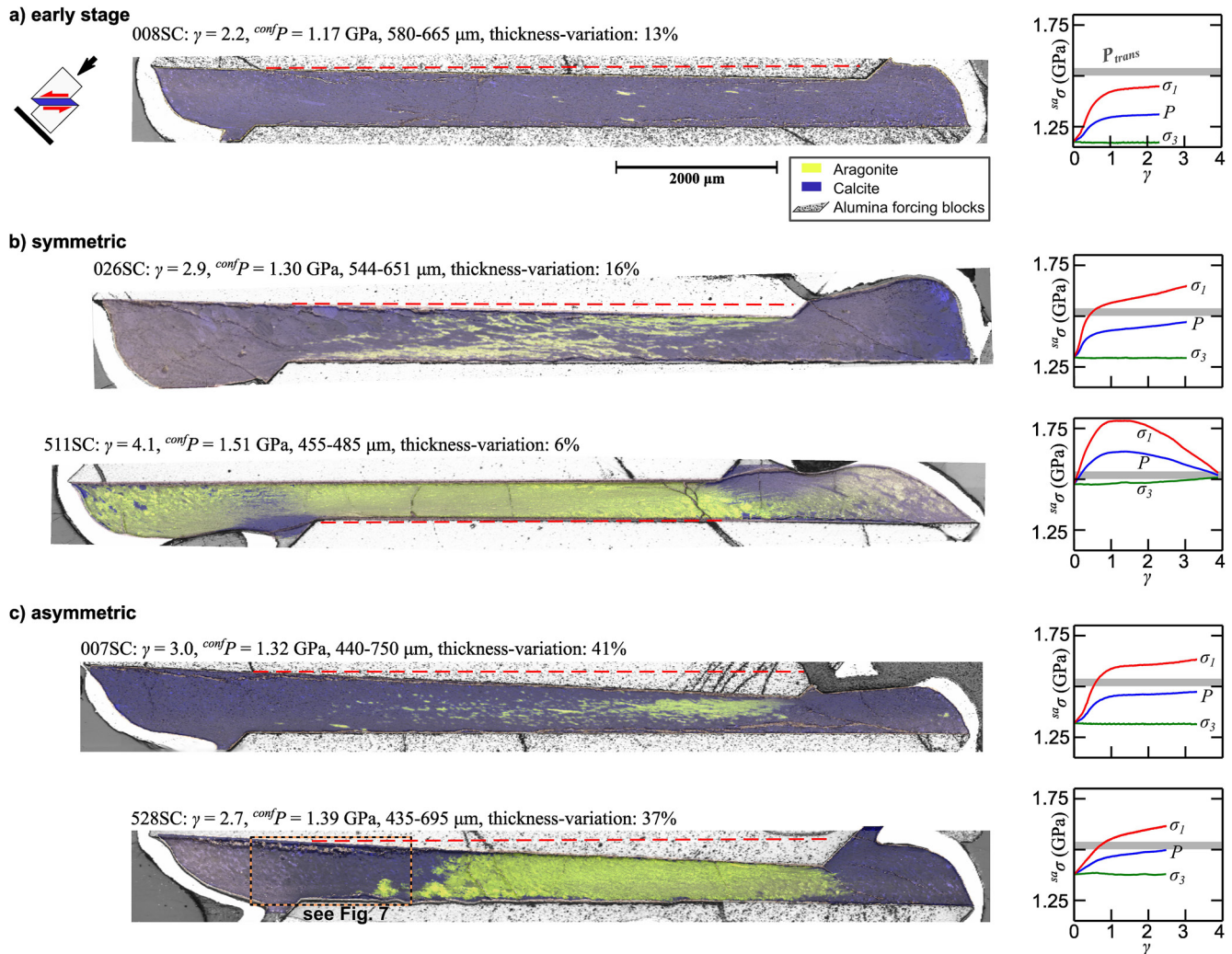


Figure 2. Experimentally produced shear zones and the corresponding sample-average stress-strain curves. The deformed samples are shown as a combination of Raman maps laid over reflected light microphotographs. The dashed red line indicates the orientation that is parallel to the opposed forcing-block interface. The insets on the right show the sample-averaged principal stress and pressure ($^{\text{sa}}\sigma_1$, $^{\text{sa}}P$, and $^{\text{sa}}\sigma_3$) evolution with increasing strain. The gray line marks P_{trans} (1.52 GPa at 600°C). Both axes are scaled equally for all plots. The sketch in the left upper corner shows the approximate location of the shear zone within the sample assembly. (a) Experiment performed at low $^{\text{conf}}P$ and stopped at $\gamma = 2.2$, showing the early stage of aragonite formation and a small asymmetry. (b) Symmetric experiments that show less variation in shear-zone thickness and a more symmetric distribution of aragonite. (c) Experiments that show asymmetrical thinning of the shear zone. Aragonite is more abundant in the thinned parts.

3. Experimental Results

In all experiments, aragonite formed at the expense of calcite to a varying extent. In fact, calcite and aragonite grains show strong local variation in shape, size, and orientation indicating variations in strain. For all experiments, the strain gradient across the shear zone is small in the core of the sample and it increases toward the tips of the shear zone. Regions of higher strain are the regions with the smallest grain-size (Figure 2 and Figure S4 in Supporting Information S1). In experiments with $\gamma > 4$, an average grain-size of 20 μm was measured in the center of the shear zone. A first abrupt and then gradual increase in grain-size (from 2 to 60 μm) along the vertical section is observed at the rims (Figure 2b).

After deformation, the observed thickness of the shear zone is not always constant, this variability appears to correlate with the original sample grain-size. The initially coarse-grained samples (e.g., 511SC and 026SC) show little thickness variation along the shear zone (Figure 2b). The initially fine-grained samples (e.g., 007SC and 528SC) exhibit asymmetrical thinning that also produced thin and thick bulges at the tips of the shear zone

(Figure 2c). The low shear strain sample 008SC (Figure 2a; $\gamma = 2.2$; asymmetry 13%) shows the initial nucleation of aragonite predominantly in the slightly thinner half of the shear zone. For this sample, both, ${}^{sa}\sigma_1$ and ${}^{sa}P$, were below the transition threshold (Figure 2a, inset). All other deformed samples experienced larger strain and sample-average stresses and can be broadly categorized as “symmetric” or “asymmetric” based on the variation of shear zone thinning (Figure 2).

3.1. Symmetric Shear Zone

The forcing blocks confining the shear zone are subparallel in the symmetric geometries (Figure 2b). The deviation of the forcing block faces from parallel is less than 1.5° (i.e., 16% thickness variation). In these experiments, aragonite is distributed almost symmetrically around the shear-zone center. In 026SC, only ${}^{sa}\sigma_1$ overstepped P_{trans} and aragonite formation is confined to the zone, where the forcing blocks overlap. In 511SC with high finite strain ($\gamma = 4$), both, ${}^{sa}P$ and ${}^{sa}\sigma_1$, exceeded P_{trans} . Here, almost all of the calcite starting material between the forcing blocks is transformed to aragonite. Interestingly, some aragonite is also found in the extruded bulges. However, an increased amount of calcite is observed in a triangular-shaped region between the extruded bulge and the confined shear zone (Figure 2b). The two samples, 511SC and 026SC, have different starting material and preparation procedure as described in Section 2 and in Table S1 in Supporting Information S1. Furthermore, sample 511SC shows the highest degree of transformation and grain-size reduction, which may be associated with significant softening behavior that is documented macroscopically (Figure 2b; inset). As the materials were not prepared employing exactly the same procedure, further investigation of this potential softening effect is beyond the scope of this study.

3.2. Asymmetric Shear Zone

In asymmetrically thinning samples, the right end of the shear zone is up to 41% thinner compared to the left end (Figure 2c). With respect to the assembly orientation, thinning is mostly observed at the upper tip of the shear zone. The asymmetric thinning of the samples is also observed in the platinum separators (cups) between pistons and forcing blocks. ${}^{sa}\sigma_1$ exceeded P_{trans} in the asymmetric samples (Figure 2c). The thinner part in these samples shows an increased formation of the high-pressure phase aragonite (Figure 2c). Specifically, in 528SC, the transition is almost complete in its thinner part, while its thicker end consists mainly of calcite. In 007SC, aragonite formation is heterogeneous in the thinned part, where an increased amount of aragonite was formed next to the upper piston right tip (Figure 2c). This region, near to the forcing block inner tip, is also characterized by reduced grain-size (Figure S4 in Supporting Information S1).

4. Modeling Results

The modeled configuration allows for the quantification of mechanical parameters for all the major components of the experimental assembly including the confining medium, the pistons/forcing blocks, and the jacket (Figures 3a and 3b). The numerical results show that the stress state of the low-viscosity confining medium (salt) is close to hydrostatic and homogeneous as expected (Figure 3b). Conversely, pressure is not homogeneous in the rest of the model during deformation (Figure 3b). This means that the state of stress within the deforming sample is not homogeneous. The numerical model results can also be used to extract the mechanical variables in a way that is emulating the experimental measurements (confining pressure, piston, and sample average stresses; see Figures 3c and 3d for details). For the comparison of sample-averaged data, we performed a piston-overlap correction in the same manner as in the processing of the experimental data (Figure 1b). Since we are only modeling the viscous deformation of the assembly, the steep stress increase of the “loading phase” is not depicted by our model. The model results are presented separately for the symmetric and the asymmetric case as it was done in the case of experimental results.

4.1. Symmetric Shear Zone

The distribution of mechanical variables is shown in relation to the locally averaged values for the case of a symmetric shear zone (Figure 4). The spatial distribution of the mechanical variables within the samples generally follows two trends in this geometry (Figures 4a and 4b). The values of σ_1 , P , and σ_3 are generally higher in the

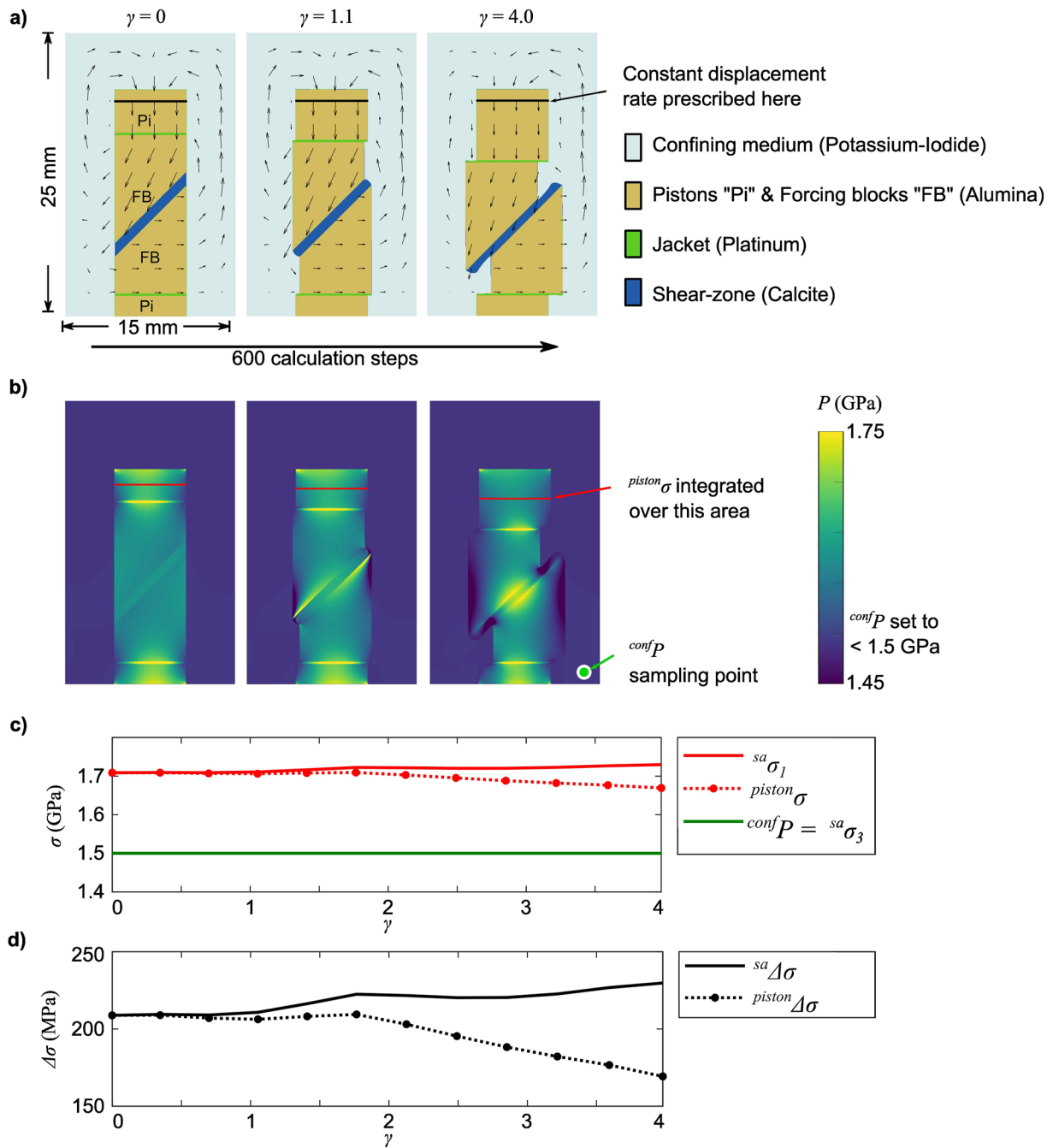


Figure 3. Overview of numerical model results. (a) Full model configuration and time evolution with increasing finite strain (γ). A constant displacement rate is defined for the upper piston (black arrows mark displacement vector field). (b) Mean stress (pressure) distribution during deformation within the model (in color). (c) Time evolution of the $^{sa}\sigma$, $^{piston}\sigma$, and ^{conf}P values. (d) Differential stress derived from the model $^{piston}\Delta\sigma$ (dotted line) and resulting $^{sa}\Delta\sigma$ (solid line) after overlap correction.

core of the sample with the maximum values being at the region of maximum overlap of the two forcing blocks (Figure 4a). These values are decreasing toward the confining medium, where they yield an almost hydrostatic stress state at the sample-confining medium interface. The results indicate that all normal stresses are higher in the core of the sample domain and their distribution is not homogeneous in such experiments. Other mechanical variables that are related to the intensity of shear deformation ($\Delta\sigma$, $\dot{\gamma}$, and γ), are also not homogeneous within the shear zone. The distribution of these variables shows increased values along the shortest diagonal that connects the two tips of the opposite forcing blocks, with lower values around the sample core and higher at the

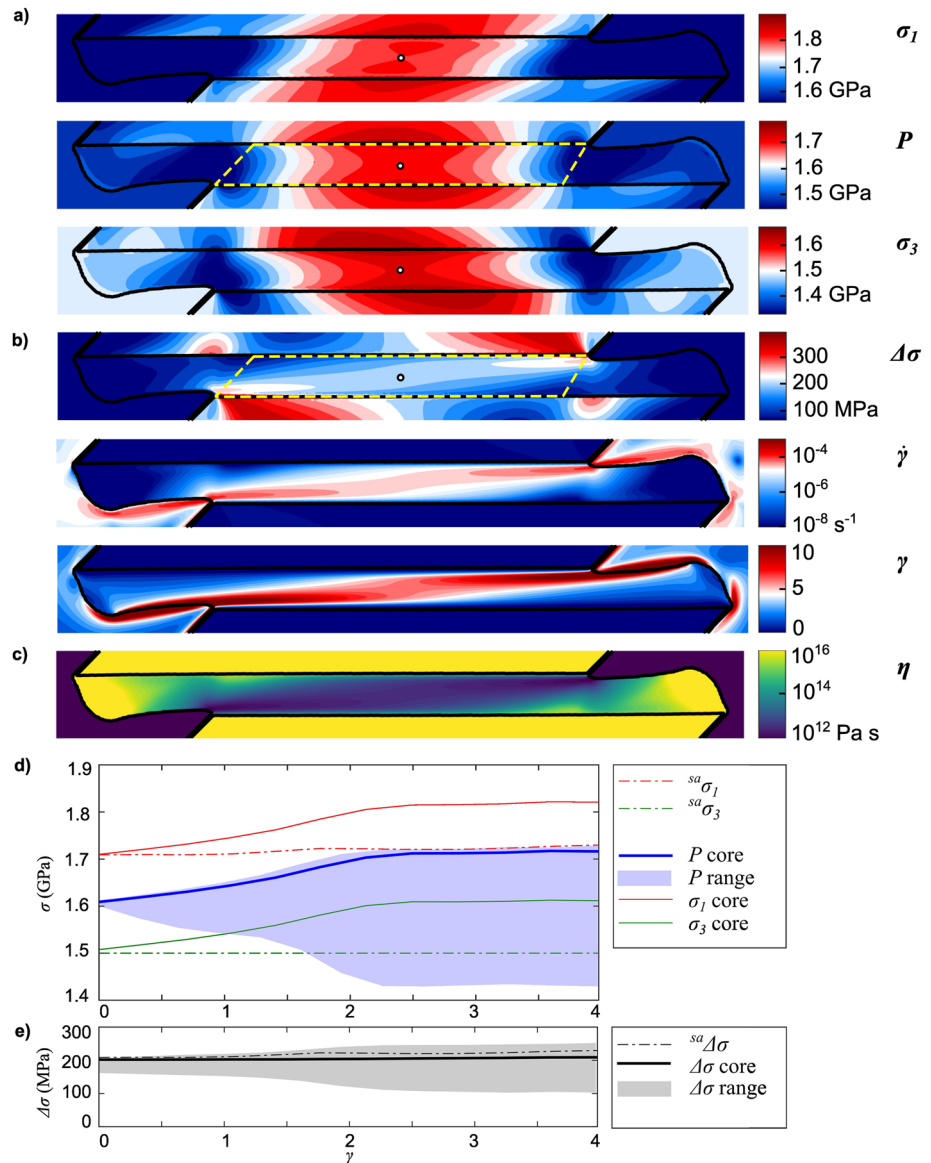


Figure 4. Results from numerical model of the experimental assembly for the case of a symmetric shear zone (e.g., 511SC). The 2D model is shown for $\gamma = 3.9$. (a, b) Distribution of mechanical variables within the shear zone (in color) and the surrounding regions (edges of the forcing blocks and confining medium). The color-bars for σ_1 , P , σ_3 , $\Delta\sigma$, $\dot{\gamma}$, and γ are centered around the sample average values which are indicated by white color. Contours for σ_1 , P , σ_3 , and $\Delta\sigma$ are calculated with a 25 MPa interval. Positive (red) and negative (blue) variations from the sample-average values are indicated. Point symbols in σ_1 , P , σ_3 , and $\Delta\sigma$ indicate the locations where the local values are monitored. (c) Distribution of the effective viscosity in the sample. (d) Stress evolution for the indicated points within the shear zone as functions of the finite strain. Additionally, the range of pressure (variation) within the shear zone (dashed yellow line in (a)) is shown. The sample-averaged values are shown for comparison. (e) Differential stress evolution for the indicated points as a function of strain. Range of variations and sample-average value as in (d).

tips (Figure 4b). The effective viscosity follows the opposite trend compared to the strain rate (Figure 4c). The comparison of the distributions of all stress variables shows that relatively high values of $\Delta\sigma$ within the sample coincide with the maximum values of P , σ_1 , and σ_3 only around the core part of the sample (compare Figures 4a and 4b). However, the highest values of $\Delta\sigma$ are found adjacent to the inner forcing blocks tips, where the value of P is close to pressure of the confining medium.

More specifically, the increase in P , σ_1 , and σ_3 from the edge of the sample toward its core can reach 250 MPa over a distance of 4 mm along the shear zone. Such an increase is larger than the magnitude of the modeled

sample-averaged differential stress (210 MPa; Figures 4a and 4e). The variations in P , σ_1 , or σ_3 are increasing with on-going deformation (increase of γ), reflecting a more pronounced heterogeneous distribution of stress within the sample. This heterogeneity is responsible for the large range of the stress values in Figures 4d and 4e. After relatively large deformation ($\gamma = 3.9$), the local values of σ_1 , P , and σ_3 are increased by ~ 120 MPa at the sample core compared to the expected sample-averaged values (Figure 4d). In contrast, for the same deformation amount, the local values of σ_1 , P , and σ_3 at the sample rim are reduced by ~ 90 MPa compared to the sample-averaged value. Interestingly, the models reveal a small triangular region between the shear zone and the extruded bulge, where the sample pressures are lower than the pressure in the confining medium (Figure 4a). In summary, the modeled geometry reveals that, at later stages of deformation ($\gamma > 2.5$), the local pressure in the central region can be as high as $^{sa}\sigma_1$. On the contrary, at the ends of the shear zone, the local pressure values can be as low or even lower than as $^{sa}\sigma_3$.

The values related to the intensity of shear deformation also show a heterogeneous distribution that amplifies with increasing deformation. For $\gamma = 3.9$ and for the present case of calcite with an average strain rate of $1.7 \cdot 10^{-5} \text{ s}^{-1}$, the central sample region (i.e., between overlapping forcing blocks) has values of local strain rates ranging from $3 \cdot 10^{-4}$ to 10^{-8} s^{-1} (Figure 4b). For a vertical section across the central region, the differential stress ranges between 150 and 200 MPa, with the highest values being at the central point of the sample (Figure 4b). In addition, the differential stress across the shear zone close to the inner tip of the forcing blocks drops from 250 MPa at the top-right side to 90 MPa at the bottom-right side (Figure 4b). These values indicate a differential stress gradient across the shear zone (e.g., vertically in Figure 4b) that is ~ 150 MPa/mm for the core region and ~ 240 MPa/mm for the shear zone edge. As a result of all the stress/strain rate variations, the effective viscosity varies by more than 1 order of magnitude within the shear zone (Figure 4b). It is important to note, that although $\Delta\sigma$ and $\dot{\gamma}$ follow the same diagonal distribution, they are nowhere simultaneously equal to the sample average values, as would be required by the homogeneous deformation assumption.

4.2. Asymmetrically Thinning Shear Zone

To reproduce the observed thickness variation of the shear zone in the experimental samples (007SC and 528SC; Figure 2c), we imposed a horizontally increasing gradient of 12% in the deformation speed of the upper piston (see Section 2 and Figure 3). This gradient is responsible for the asymmetric velocity field and results in the uneven thinning of the modeled shear zone. The numerically produced shear zone is 25% thinner on its right tip compared to its left tip at the final deformation stage (Figure 5). Similar to the symmetric case, the distribution of the mechanical variables follows two trends. σ_1 , P , and σ_3 have the largest values at the core of the shear zone where the overlap region of the forcing blocks is maximal (Figure 5a). $\Delta\sigma$, $\dot{\gamma}$, and γ are also heterogeneously distributed, with the relatively high values being along the shortest diagonal that connects the two forcing blocks (Figure 5b). Due to its strain rate sensitivity, the effective viscosity is relatively lower at the same diagonal as it was observed in the symmetric models (Figure 5c).

The model results reveal that, despite the similar trends in mechanical variables, the asymmetric shear zone has maxima of σ_1 , P , and σ_3 that are shifted toward the thin part of the shear zone (Figure 5a). Furthermore, the large values of $\Delta\sigma$, $\dot{\gamma}$, and γ along the shortest diagonal are slightly more pronounced on the thin (right) side of the shear zone (Figure 5b). Similar to the symmetric shear zone model, all spatial variations in mechanical variables amplify with the progression of deformation. This amplification is reflected by the scatter of the time-evolution curves in Figures 5d and 5e. These curves show that the pressure within the shear zone can reach values that are larger than $^{sa}\sigma_1$ and smaller than $^{sa}\sigma_3$ (Figure 5d). Thus, the pressure variation along the shear zone in such experiments is larger than $^{sa}\Delta\sigma$ (Figures 5a, 5d and 5e). Interestingly, the pressure in the core of the shear zone is almost identical in value to the $^{sa}\sigma_1$ at strains greater than 2.5 (Figure 5d). Differential stresses within the shear zone also show an increasing variation over time with the largest values being ~ 250 MPa and the lowermost values being ~ 110 MPa (after $\gamma > 2.5$), both at the thin side of the shear zone (Figure 5e).

5. Comparison of Experimental and Modeled Stress Values

The produced numerical model was validated against the presented experimental samples using both qualitative (shape and distribution) and quantitative (stress and grain-size measurements) criteria. To a first order, the numerical model captures the geometrical evolution of the deforming sample well (e.g., Figure 3). In a more

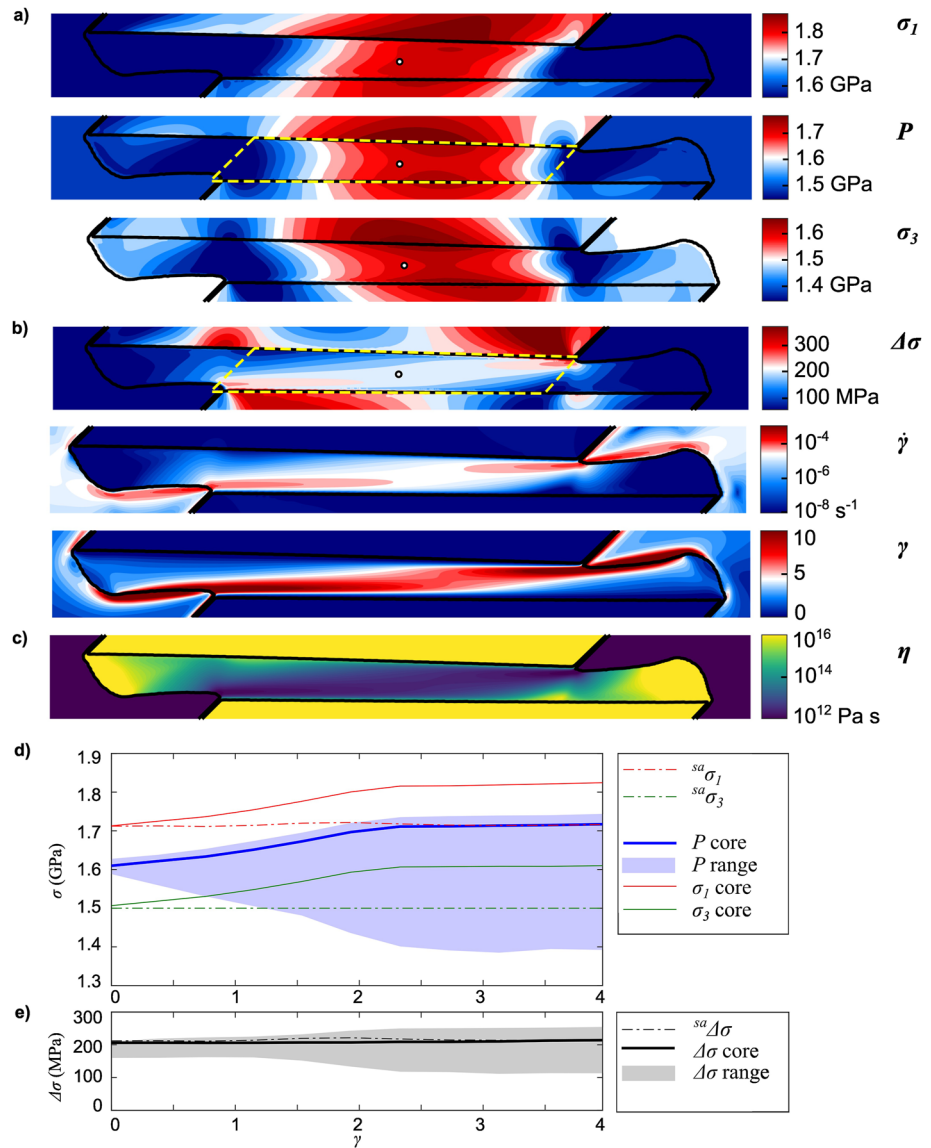


Figure 5. Results from numerical model of the experimental assembly for the case of an asymmetric shear zone (e.g., 528SC). The 2D model is shown for $\gamma = 3.9$. The description for (a)–(e) is identical as in Figure 4.

quantitative way, the numerically produced sample average stress and strain rates are compared to the corresponding experimental values.

The experimentally measured peak $\Delta\sigma$ ranges between 250 and 350 MPa, and the modeled $\Delta\sigma$ varies around 205 MPa for both, symmetric and asymmetric, geometries. However, the numerical models are based on flow laws determined in a gas apparatus (Schmid et al., 1980). Such data can be compared with Griggs-type experiments only if an additional calibration is applied (correction factor = 0.73; Holyoke & Kronenberg, 2010). Applying the inter-apparatus calibration raises the numerically determined stresses by 80–140 MPa, varying with the assembly type (Figure 6). The potassium-iodide assembly used here is both, softer than NaCl and stronger than molten salt. Therefore, any remaining difference between model and experiments is within error.

The inhomogeneity of stress, strain, and strain rate in deformation experiments is quite common and can be observed in many cases such as the necking of metal rods under tension, barreling in compression, or shear band formation in rock or soil. The inhomogeneous strain/stress distribution makes the stress-strain curves no longer objective for the characterization of material behavior (Vermeer & De Borst, 1984, p. 13). Thus, if the role of

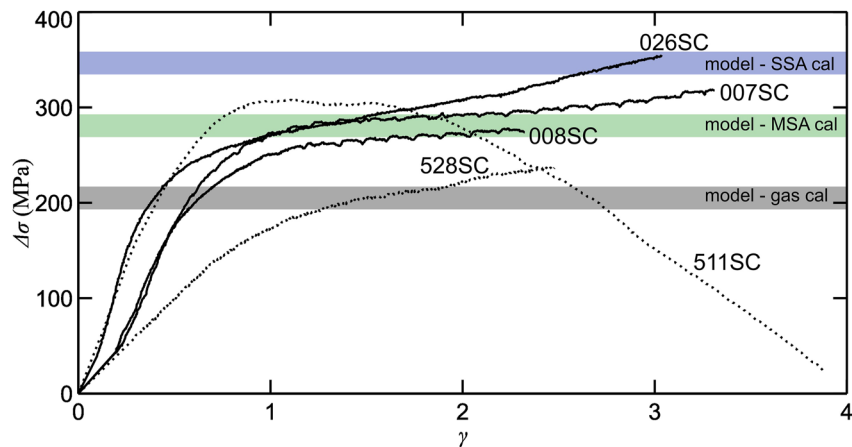


Figure 6. Stress-strain curves of the analyzed samples in comparison to numerical modeling results obtained using a flow law calibrated in a gas-apparatus (model gas cal). We apply the calibrations of Holyoke and Kronenberg (2010) to the modeling results: Molten salt assembly (MSA) and solid salt assembly (SSA—calibrated using NaCl), see main text for details. The strength of the potassium-iodide assembly ranges in between these two (Inoue, 1957; Pec et al., 2012). A generally good fit between model prediction and experimental results is observed. For stress-strain curves of all experiments done see Figure S5 in Supporting Information S1.

stress as a thermodynamic potential is investigated, an accurate description of the state of stress is needed. The distribution of differential stress within the sample may not be known during the experiment. However, we can use the resulting grain-size distribution from the experimentally deformed samples as a proxy for the level of differential stress distribution based on grain-size piezometry (for calcite: e.g., Rutter, 1995). The general relation is that the recrystallized grain-size can be inversely related to the differential-stress level. Figure 7a illustrates that the grain-size in the experimentally deformed sample is not homogeneous. There is a distinct gradient with the smaller grains being observed at the tip of the lower forcing block and increasing grain-sizes being observed toward the opposing (upper) forcing block (Figure 7a), where the strain decreases to almost 0. The average grain-size increases from few microns adjacent to the forcing block tip to ca. 20–40 μm at the “upper” low-strain-end. This is documented by the increasing mode of the grain-size distribution analysis done for each half individually (Figure 7b). The modeled differential stress for the region, where the EBSD map was done, correlates with the increase of stress inferred from the grain-size variations across the shear zone in the analyzed region (Figures 7a and 7c). A more quantitative comparison of the experimental grain-sizes with model results calculated from differential stress and already published piezometers are shown in Figure S6 in Supporting Information S1.

It is important to note, that the relative magnitude of local stress/pressure/strain variations presented here is strongly dependent on the aspect ratio of the shear zone. Increasing the thickness (for a given length), will lead to less pronounced spatial variations.

6. Discussion and Conclusions

We performed calcite deformation experiments and numerical models to simulate its behavior near the calcite-aragonite phase transition. All experimental samples show aragonite formation locally that resulted in a heterogeneous distribution of the two CaCO₃ polymorphs. In addition, numerical models were developed and used to provide insights into the distribution of local mechanical parameters during sample deformation. The modeled principal stresses, pressure, differential stress, and deformation rates also show heterogeneous patterns as observed in the experimentally produced phase and grain-size distribution. In fact, in experimental studies, it is common to observe shear bands and zones of localized deformation not randomly distributed but rather following specific patterns (Holtzman et al., 2003; Marti et al., 2020; Pec & Al Nasser, 2021; Pec et al., 2016). In this work, we showed that the distribution of shear stress and strain is more pronounced along the short diagonal in the central part of the sample, that links the forcing-block inner tips. These results highlight the importance of local stress distribution within the deforming sample.

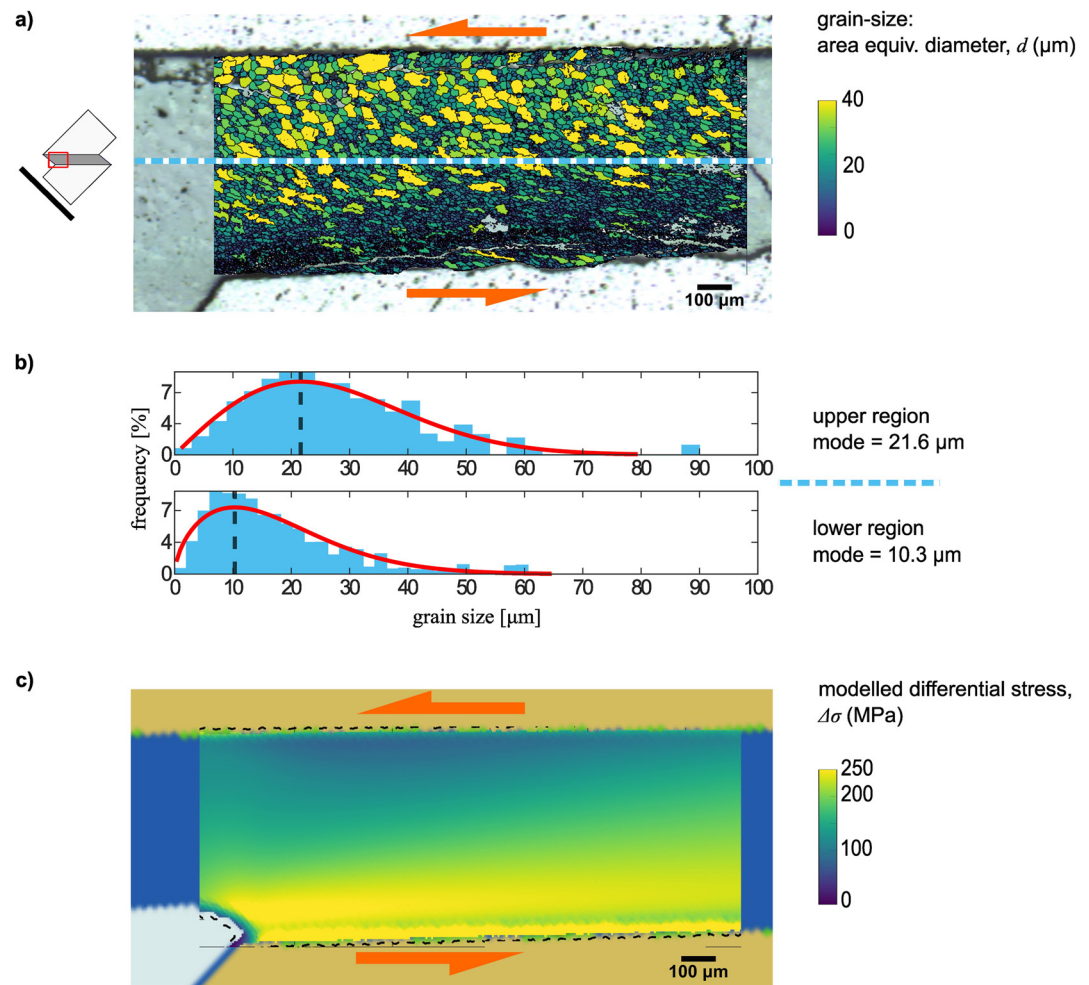


Figure 7. Experimental grain-size and modeled differential stress distribution. (a) EBSD map of sample 528SC (left edge), where the grain-size of calcite was measured. The photomicrograph from Figure S4 in Supporting Information S1 is shown in the background). The dashed blue line separates the two regions used for the grain-size distribution overview in (b). (b) Grain-size distribution in the upper and lower half of the mapping domains. The mode of the grain-size distribution in each region is indicated by vertical dashed lines. (c) Differential stress calculated by the mechanical model for asymmetric samples (see Figure 5) for the same sample-averaged stress/strain values and geometrical configuration as in (a).

The experimental results can be broadly categorized based on the extent of asymmetric thinning experienced by the shear zone. In the symmetrical case, the locations of formation of aragonite coincide with the distribution of total strain if the sample averaged σ_1 oversteps the phase transition and the sample averaged pressure gets close to it (Figures 2 and 4). However, in samples with asymmetric shear zones the formation of aragonite is limited to the regions of high local pressure (Figures 2 and 5). This is the thinned part of the shear zones, where the pressure is expected to be higher based on results from numerical models. Within the high-pressure region, the formation of aragonite follows the high strain in some experiments (e.g., 007SC), in others (026SC), the entire high-pressure region is transformed into aragonite. Importantly, no aragonite is formed in the low-pressure region, despite high strain.

The comparison of experiments and numerical models indicates that the formation of aragonite is controlled by the spatial distribution of mechanical parameters. It has been suggested that mechanical work produced plays a crucial role in the formation of fine-grained or amorphous materials during deformation (Austin & Evans, 2007; Pec & Al Nasser, 2021). The enhancing kinetic effect of deformation on reaction progress has been demonstrated by de Ronde and Stünitz (2007) and Richter et al. (2016). As shown in Figure S7 in Supporting Information S1, the dissipative work per unit time (the product of stress and viscous strain rate) is relatively large close to the forcing-blocks inner tips and links these along the short diagonal, where the differential stress and strain rate are

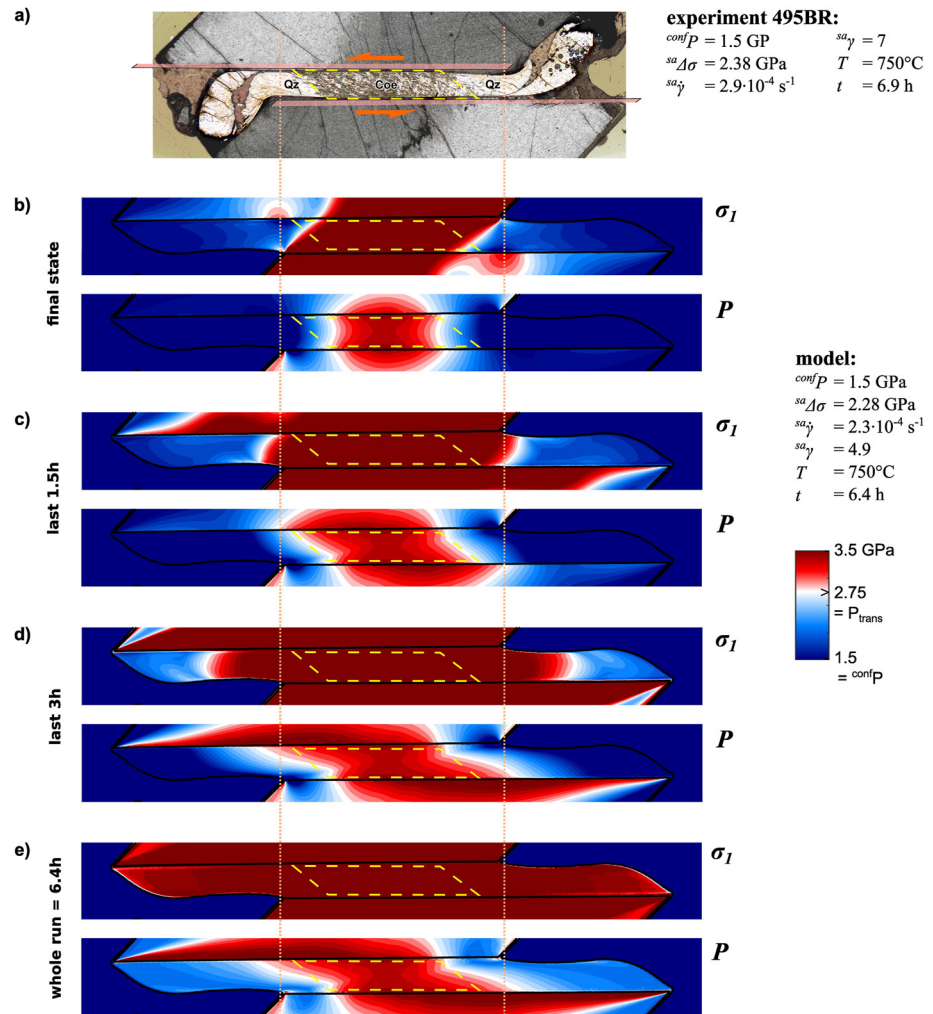


Figure 8. Comparison of the deformation experiment 495BR in SiO_2 system (Richter et al., 2016) with numerical models for σ_1 and P . (a) Reflected light photomicrograph of the experiment, clearly showing coesite formation by increased relief (darker grains). The zone of coesite occurrence is outlined by the dashed yellow line. Qz = quartz and Coe = coesite. (b)–(e) Distribution of σ_1 and P within the shear zone and the surrounding regions (edges of the forcing blocks and confining medium) for varying time increments of the experimental run. The color-bar ranges around the Qz–Coe phase transition pressure, which is characterized by white color. Contours are calculated with a 100 MPa interval. The outline of Coe-bearing zone in (a) is superimposed on all models. The red color indicates that Coe formation is expected. The best fit is evaluated based on comparison of the dashed yellow area in experiments (b)–(e) and the Coe region in (a). According to numerical models of differential stress and strain, see Figure S8 in Supporting Information S1.

high. However, local high P values are necessary for the formation of aragonite. Strain appears to enhance or speed up the formation of aragonite within the regions but only where local P oversteps P_{trans} . This can be demonstrated by two key observations. On the one hand, aragonite is not present in all the regions that have experienced high strain, and, on the other hand, aragonite is present (to a varying extent) in all regions that have experienced high local pressure (mean stress). Furthermore, strain seems to predominantly enhance the phase transition only when the local pressure overstepping is low (007SC and 026SC). With increasing degree of pressure overstepping, the role of strain decreases (511SC and 528SC). Interestingly, our results agree with the previous interpretation of quartz-to-coesite experiments that highlighted the occurrence of high-pressure polymorphs also in the low-strain regions (strain shadows; Ji & Wang, 2011). The main differences between our experiments and the experiments interpreted by Ji and Wang (2011) are: (a) the composition of the system (CaCO_3 instead of SiO_2) and (b) the experimental configuration (general shear instead of coaxial shortening). However, to investigate the applicability of our modeling approach, we also simulated the experiments of Richter et al. (2016), who considered the SiO_2 system (quartz-to-coesite transition) under general-shear conditions (Figure 8a). Due to material properties, the

differential stress sustained by SiO_2 polymorphs is generally larger than for CaCO_3 polymorphs. The large values of differential stress lead to smaller uncertainties in experimental data and therefore the role of non-hydrostatic stresses will be more pronounced. As previously documented by Richter et al. (2016), coesite formation occurred in experiments during which $^{\text{ax}}\sigma_1$ reached the coesite field. However, when analyzing the distribution of coesite, we observed that increased amounts of coesite are found in the center of symmetric shear zones (e.g., 495BR; Figure 8a). Our numerical model for this experiment predicts instantaneous pressure values in the center of the shear zone that go beyond the phase-transition pressure toward the end of the experiment (Figure 8b).

In fact, there are two main factors that need to be considered in the interpretation of the phase transitions. One is the driving force for the reaction, which would guarantee the sufficient degree of overstepping of the phase transition. The second important factor is the role of the kinetics of the phase transition (henceforth “kinetics”). Theoretically, in the limiting case with instantaneous equilibration, kinetics is infinitely fast and therefore the experiment could be characterized solely by the distribution of its mechanical variables (e.g., stress and pressure) at the end of the experiment, before quenching. If kinetics were infinitely fast, the final stage of the model (Figure 8b) would have to be identical to the experimental observation (Figure 8a). In reality, all kinetic processes are characterized by a finite timescale. This means that even if a system is brought to conditions that would favor the nucleation of a new phase, the system would still need a finite amount of time to respond. Experimental data from Hirth and Tullis (1994) focused on the quartz to coesite transition during coaxial shortening experiments showed that the transformation took place only at temperatures above $\sim 600^\circ\text{C}$ and the rates of transformation were too slow below that value. This dependency on the degree of transformation and the temperature of the experiment was later confirmed by Richter et al. (2016) for the general-shear deformation. These observations document that, for a given temperature, there is a finite amount of time that is needed for the transformation to take place (both forward and backward). Therefore, the actual phase distribution at the end of the experiment may not correspond to an instantaneous equilibrium phase distribution but may be rather influenced by the history of the sample's stress/pressure/strain, and so on. To overcome the unknown time scale related to kinetics, we can examine the evolution of the mechanical variables for given time frames. In this way, we can identify which mechanical parameter is the key driver that guarantees the necessary degree of overstepping by comparison with the experimental results (Figure 8c).

We monitored the maximum values of given parameters (pressure, σ_1 , strain, strain rate, etc.) that are experienced by every “particle” (i.e., Lagrangian marker) of our model for a given amount of time while tracing its movement across the model domain. This time and space resolved monitoring reveals that a material point will experience a variety of conditions as a result of the evolving geometry. Here, we focus on pressure and σ_1 because they seem to have the greatest impact on the distribution of the polymorphs in the calcite/aragonite case. Differential stress and strain evolution are provided in Figure S8 in Supporting Information S1. We chose to plot the maximum pressure/stress value experienced by every “particle” of the model for the last 1.5, 3.0, and 6.4 hr of the experiment (Figures 8c–8e). Since the experiment lasted for 6.4 hr, this corresponds to the whole duration of the experiment. The last 3.0 hr corresponds to the last $\sim 46\%$ of the duration and the last 1.5 hr corresponds to the last $\sim 23\%$ of the duration of the experiment. In other words, the reported values in Figures 8c–8e correspond to the maximal values of σ_1 and pressure a given particle (which is now shown in its final position) experienced on its way during a given period.

With this approach, we are able to investigate if a particular part of the model domain experienced conditions above the phase-transition pressure and did not back-react due to kinetic reasons. The main reason for back-reactions is that the geometry of the samples keeps evolving and therefore the stress distribution keeps changing. Our results show that in all cases (1.5, 3.0, and 6.4 hr), only pressure can be related to the phase distribution of coesite observed in the experiment. Interestingly, using the local σ_1 values does not seem to reproduce any of the patterns observed in the experiment (Figure 8). Thus, by considering the finite amount of time needed for the kinetics of the reaction, the results of this test suggest that local pressure values are responsible for the transformation. Similar to the calcite/aragonite case, strain enhances the quartz/coesite transition and the back-reaction, especially when the degree of overstepping is low. However, where local P is lower than P_{trans} , no coesite was formed irrespective of the amount of strain within these domains (close to the inner piston tips, see Figure 8 and Figure S8 in Supporting Information S1). This observation can be used to rule out local σ_1 as a driving force for phase transitions. For example, if σ_1 was controlling the phase transition, coesite should be observed in regions with local high σ_1 and strain (the region at the inner piston tips; Figure 8 and Figure S8 in

Supporting Information S1). However, the experimental sample 495BR of Richter et al. (2016; also Figure 8a) does not support this interpretation.

Previous studies suggested that the maximum principal stress can be used as a thermodynamic potential for reactions in the presence of differential stress (e.g., Hirth & Tullis, 1994). Based on the stress magnitude in the presented models (Figures 4 and 5), and in contrast to the theoretical works of Wheeler (2014, 2020), the correlation between maximum sample averaged principal stress and phase transformation may not be interpreted as a causal relationship for such experiments. This is particularly important if the role of stress as a thermodynamic potential is under investigation. In any differentially stressed sample, its geometry leads to stress concentrations (despite of homogeneous sample material)—this is true for general shear as shown here, but also for coaxial shortening (e.g., Ji & Wang, 2011). In these samples, large values of sample-averaged differential stress ($\Delta\sigma$) will result in large magnitudes of spatial pressure (i.e., mean stress) variations. Such variations can drive mineral reactions and phase transitions locally (e.g., Moulas et al., 2013).

At this point, we should make clear that the role of stress in mineral reactions can be direct or indirect. A direct effect of stress on phase equilibria is the displacement of pressure and temperature (P - T) conditions, where phases coexist (Frolov & Mishin, 2010; Sekerka & Cahn, 2004). Note that this effect exists even if the stress distribution within each reacting phase is homogeneous. In contrast, the indirect role of stress would be the formation of spatially variable pressure/stress patterns or concentrations that would undeniably change—locally—the free energy of the reacting mixture. Based on the high-stress gradients in viscously deforming polycrystalline material within our experiments and models (100 MPa/mm to GPa/mm), the homogeneous stress assumption may not be appropriate. Therefore, these local changes in energy should be considered in addition to local contributions from deviatoric stress/strain tensor components. For this reason, without the knowledge of the stress distribution in the sample, it is impossible to assess the role of stress in mineral reactions. Interestingly, local stress variations that may result from heterogeneous mechanical properties and the geometrical configuration are not restricted to the experiments only, but also relevant for natural settings (Jamtveit et al., 2018; Luisier et al., 2019; Moulas et al., 2022; Putnis et al., 2021).

To conclude, we demonstrated that the coupled use of experiments and numerical modeling can provide important insights in the role of stress on mineral reactions. Currently, experimental measurements do not provide any information on the spatial distribution of mechanical variables within the sample (except for experiments monitored live in synchrotron facilities). Therefore, the use of accurate mechanical models resolving spatially varying mechanical parameters is necessary. Alternatively, new kinds of experiments are needed that would be able to resolve the mineral reactions in situ during deformation.

Conflict of Interest

The authors declare no conflicts of interest relevant to this study.

Data Availability Statement

All data (Griggs-run-data, Raman, EBSD) for this research are available at Zenodo: <https://doi.org/10.5281/zenodo.6974768>. Software for this research is available in the in-text data citation reference: Cionoiu et al. (2022). The code is licensed following “Creative Commons Attribution 4.0 International.”

Acknowledgments

S.C. acknowledges ETH research Grant 38 15-1; E.M., S.C. and L.T. acknowledge support by the Excellence cluster funding of the Heidelberg University for “Hei-D lab”, the experimental deformation lab. The authors thank Yves Bernabe for his editorial work. The authors greatly appreciate the constructive reviews by one anonymous reviewer and Matej Pec, which have improved the clarity of this paper. Open Access funding enabled by the project DEAL.

References

- Austin, N. J., & Evans, B. (2007). Paleowattmeters: A scaling relation for dynamically recrystallized grain size. *Geology*, 35(4), 343. <https://doi.org/10.1130/G23244A.1>
- Barnhoorn, A., Bystricky, M., Burlini, L., & Kunze, K. (2004). The role of recrystallisation on the deformation behaviour of calcite rocks: Large strain torsion experiments on Carrara marble. *Journal of Structural Geology*, 26(5), 885–903. <https://doi.org/10.1016/j.jsg.2003.11.024>
- Biellmann, C., & Gillet, P. (1992). High-pressure and high-temperature behaviour of calcite, aragonite and dolomite: A Raman spectroscopic study. *European Journal of Mineralogy*, 4, 389–394. <https://doi.org/10.1127/ejm/4/2/0389>
- Cionoiu, S., Moulas, E., & Tajčmanová, L. (2019). Impact of interseismic deformation on phase transformations and rock properties in subduction zones. *Scientific Reports*, 9(1), 19561. <https://doi.org/10.1038/s41598-019-56130-6>
- Cionoiu, S., Moulas, E., & Tajčmanová, L. (2022). Local variation of mechanical parameters in (Griggs-type) viscous deformation experiments (Matlab code). *Zenodo*. <https://doi.org/10.5281/zenodo.6951760>

- de Ronde, A. A., & Stünitz, H. (2007). Deformation-enhanced reaction in experimentally deformed plagioclase-olivine aggregates. *Contributions to Mineralogy and Petrology*, 153(6), 699–717. <https://doi.org/10.1007/s00410-006-0171-7>
- Frolov, T., & Mishin, Y. (2010). Effect of non-hydrostatic stresses on solid fluid equilibrium. I. Bulk thermodynamics. *Physical Review B*, 82, 174113. <https://doi.org/10.1103/PhysRevB.82.174113>
- Frost, H. J., & Ashby, M. F. (1982). *Deformation mechanism maps: The plasticity and creep of metals and ceramics*. Pergamon Press. <http://publications.eng.cam.ac.uk/372960/>
- Gerya, T. V. (2009). *Introduction to numerical geodynamic modelling*. Cambridge University Press.
- Gerya, T. V., & Yuen, D. A. (2003). Characteristics-based marker-in-cell method with conservative finite-differences schemes for modeling geological flows with strongly variable transport properties. *Physics of the Earth and Planetary Interiors*, 140(4), 293–318. <https://doi.org/10.1016/j.pepi.2003.09.006>
- Green, H. W. (1972). Metastable growth of coesite in highly strained quartz. *Journal of Geophysical Research*, 77(14), 2478–2482. <https://doi.org/10.1029/JB077i014p02478>
- Griggs, D. (1940). Experimental flow of rocks under conditions favoring recrystallization. *Bulletin of the Geological Society of America*, 51(7), 1001–1022. <https://doi.org/10.1130/GSAB-51-1001>
- Hacker, B. R., & Kirby, S. H. (1993). High-pressure deformation of calcite marble and its transformation to aragonite under non-hydrostatic conditions. *Journal of Structural Geology*, 15(9–10), 1207–1222. [https://doi.org/10.1016/0191-8141\(93\)90164-6](https://doi.org/10.1016/0191-8141(93)90164-6)
- Heilbronner, R., Stünitz, H., Précigout, J., & Raimbourg, H. (2020). *The solid medium deformation apparatus – reloaded (No. EGU2020-9859)*. Copernicus Meetings. EGU2020. <https://doi.org/10.5194/egusphere-egu2020-9859>
- Hielscher, R., & Schaeben, H. (2008). A novel pole figure inversion method: Specification of the MTEX algorithm. *Journal of Applied Crystallography*, 41(6), 1024–1037. <https://doi.org/10.1107/S0021889808030112>
- Hirth, G., & Tullis, J. (1994). The brittle-plastic transition in experimentally deformed quartz aggregates. *Journal of Geophysical Research*, 99(B6), 11731–11747. <https://doi.org/10.1029/93JB02873>
- Hobbs, B. E. (1968). Recrystallization of single crystals of quartz. *Tectonophysics*, 6(5), 353–401. [https://doi.org/10.1016/0040-1951\(68\)90056-5](https://doi.org/10.1016/0040-1951(68)90056-5)
- Holtzman, B. K., Kohlstedt, D. L., Zimmerman, M. E., Heidelbach, F., Hiraga, T., & Hustoft, J. (2003). Melt segregation and strain partitioning: Implications for seismic anisotropy and mantle flow. *Science*, 301(5637), 1227–1230. <https://doi.org/10.1126/science.1087132>
- Holyoke, C. W., & Kronenberg, A. K. (2010). Accurate differential stress measurement using the molten salt cell and solid salt assemblies in the Griggs apparatus with applications to strength, piezometers and rheology. *Tectonophysics*, 494(1–2), 17–31. <https://doi.org/10.1016/j.tecto.2010.08.001>
- Inoue, K. (1957). The strength of single crystals of inorganic salts under high pressure, II. *Review of Physical Chemistry of Japan*, 27(2), 54–58.
- Jamtveit, B., Moulas, E., Andersen, T. B., Austrheim, H., Corfu, F., Petley-Ragan, A., & Schmalholz, S. M. (2018). High pressure metamorphism caused by fluid induced weakening of deep continental crust. *Scientific Reports*, 8(1), 17011. <https://doi.org/10.1038/s41598-018-35200-1>
- Ji, S., & Wang, Q. (2011). Interfacial friction-induced pressure and implications for the formation and preservation of intergranular coesite in metamorphic rocks. *Journal of Structural Geology*, 33(2), 107–113. <https://doi.org/10.1016/j.jsg.2010.11.013>
- Johannes, W., & Puhán, D. (1971). The calcite-aragonite transition, reinvestigated. *Contributions to Mineralogy and Petrology*, 31(1), 28–38. <https://doi.org/10.1007/BF00373389>
- Karato, S. (2008). *Deformation of Earth materials: An introduction to the rheology of solid earth*. Cambridge University Press, 463, 2095–2096. <https://doi.org/10.1007/s00024-009-0536-8>
- Luisier, C., Baumgartner, L., Schmalholz, S. M., Siron, G., & Vennemann, T. (2019). Metamorphic pressure variation in a coherent Alpine nappe challenges lithostatic pressure paradigm. *Nature Communications*, 10(1), 4734. <https://doi.org/10.1038/s41467-019-12727-z>
- Marti, S., Stünitz, H., Heilbronner, R., & Plümper, O. (2020). Amorphous material in experimentally deformed mafic rock and its temperature dependence: Implications for fault rheology during aseismic creep and seismic rupture. *Journal of Structural Geology*, 138, 104081. <https://doi.org/10.1016/j.jsg.2020.104081>
- Moulas, E., Kaus, B., & Jamtveit, B. (2022). Dynamic pressure variations in the lower crust caused by localized fluid-induced weakening. *Communications Earth & Environment*, 3(1), 1–7. <https://doi.org/10.1038/s43247-022-00478-7>
- Moulas, E., Podladchikov, Y. Y., Aranovich, L. Y., & Kostopoulos, D. (2013). The problem of depth in geology: When pressure does not translate into depth. *Petrology*, 21(6), 527–538. <https://doi.org/10.1134/S0869591113060052>
- Moulas, E., Schmalholz, S. M., Podladchikov, Y., Tajčmanová, L., Kostopoulos, D., & Baumgartner, L. (2019). Relation between mean stress, thermodynamic, and lithostatic pressure. *Journal of Metamorphic Geology*, 37(1), 1–14. <https://doi.org/10.1111/jmg.12446>
- Paterson, M. S. (1973). Nonhydrostatic thermodynamics and its geologic applications. *Reviews of Geophysics*, 11(2), 355. <https://doi.org/10.1029/RG011i002p00355>
- Paterson, M. S., & Wong, T. (2005). *Experimental rock deformation – the brittle field*. Springer Science & Business Media.
- Pec, M., & Al Nasser, S. (2021). Formation of nanocrystalline and amorphous materials causes parallel brittle-viscous flow of crustal rocks: Experiments on quartz-feldspar aggregates. *Journal of Geophysical Research: Solid Earth*, 126(5), e2020JB021262. <https://doi.org/10.1029/2020JB021262>
- Pec, M., Stünitz, H., & Heilbronner, R. (2012). Semi-brittle deformation of granitoid gouges in shear experiments at elevated pressures and temperatures. *Journal of Structural Geology*, 38, 200–221. <https://doi.org/10.1016/j.jsg.2011.09.001>
- Pec, M., Stünitz, H., Heilbronner, R., & Drury, M. (2016). Semi-brittle flow of granitoid fault rocks in experiments. *Journal of Geophysical Research: Solid Earth*, 121(3), 1677–1705. <https://doi.org/10.1002/2015JB012513>
- Platt, J. P., & De Bresser, J. H. P. (2017). Stress dependence of microstructures in experimentally deformed calcite. *Journal of Structural Geology*, 105, 80–87. <https://doi.org/10.1016/j.jsg.2017.10.012>
- Poirier, J.-P. (1985). *Creep of crystals*. Cambridge University Press.
- Pollard, D. D., & Fletcher, R. C. (2005). *Fundamentals of structural geology*. Cambridge University Press.
- Putnis, A., Moore, J., Prent, A. M., Beinlich, A., & Austrheim, H. (2021). Preservation of granulite in a partially eclogitized terrane: Metastable phenomena or local pressure variations? *Lithos*, 400–401, 106413. <https://doi.org/10.1016/j.lithos.2021.106413>
- Redfern, S. A. T., Salje, E., & Navrotsky, A. (1989). High-temperature enthalpy at the orientational order-disorder transition in calcite: Implications for the calcite/aragonite phase equilibrium. *Contributions to Mineralogy and Petrology*, 101, 479–484. <https://doi.org/10.1007/bf00372220>
- Richter, B., Stünitz, H., & Heilbronner, R. (2016). Stresses and pressures at the quartz-to-coesite phase transformation in shear deformation experiments. *Journal of Geophysical Research: Solid Earth*, 121(11), 8015–8033. <https://doi.org/10.1002/2016JB013084>
- Richter, B., Stünitz, H., & Heilbronner, R. (2018). The brittle-to-viscous transition in polycrystalline quartz: An experimental study. *Journal of Structural Geology*, 114, 1–21. <https://doi.org/10.1016/J.JSG.2018.06.005>

- Rutter, E. H. (1995). Experimental study of the influence of stress, temperature, and strain on the dynamic recrystallization of Carrara marble. *Journal of Geophysical Research*, *100*(B12), 24651–24663. <https://doi.org/10.1029/95JB02500>
- Rybacki, E., Konrad, K., Renner, J., Wachmann, M., Stöckhert, B., & Rummel, F. (2003). Experimental deformation of synthetic aragonite marble. *Journal of Geophysical Research*, *108*(B3), 2174. <https://doi.org/10.1029/2001JB000694>
- Schmid, S. M., Paterson, M. S., & Boland, J. N. (1980). High temperature flow and dynamic recrystallization in Carrara marble. *Tectonophysics*, *65*(3–4), 245–280. [https://doi.org/10.1016/0040-1951\(80\)90077-3](https://doi.org/10.1016/0040-1951(80)90077-3)
- Sekerka, R. F., & Cahn, J. W. (2004). Solid–liquid equilibrium for non-hydrostatic stress. *Acta Materialia*, *52*(6), 1663–1668. <https://doi.org/10.1016/j.actamat.2003.12.010>
- Tullis, T. E., & Tullis, J. (1986). Experimental rock deformation techniques. *Mineral and rock deformation: Laboratory Studies* (Vol. 36, pp. 297–324). <https://doi.org/10.1029/gm036p0297>
- Turcotte, D. L., & Schubert, G. (2014). *Geodynamics*. Cambridge University Press.
- Vermeer, P., & De Borst, R. (1984). Non-associated plasticity for soils, concrete and rock. *HERON*, *29*(3). <http://repository.tudelft.nl:80/islandora/object/uuid:4ee188ab-8ce0-4df3-adf5-9010ebfaabf0/datastream/OBJ/view>
- Wheeler, J. (2014). Dramatic effects of stress on metamorphic reactions. *Geology*, *42*(8), 647–650. <https://doi.org/10.1130/G35718.1>
- Wheeler, J. (2020). A unifying basis for the interplay of stress and chemical processes in the Earth: Support from diverse experiments. *Contributions to Mineralogy and Petrology*, *175*(12), 116. <https://doi.org/10.1007/s00410-020-01750-9>
- Zhou, Y., He, C., Song, J., Ma, S., & Ma, J. (2005). An experiment study of quartz-coesite transition at differential stress. *Chinese Science Bulletin*, *50*(5), 446–451. <https://doi.org/10.1007/BF02897461>